2021 43rd Annual International Conference of the
IEEE Engineering in Medicine & Biology Society (EMBC)
Oct 31 - Nov 4, 2021. Virtual Conference

Assessing different approaches to estimate single-subject metabolic connectivity from dynamic [^{18}F]fluorodeoxyglucose Positron Emission Tomography data

Tommaso Volpi, Erica Silvestri, Maurizio Corbetta, Alessandra Bertoldo

Abstract—**Metabolic connectivity is conventionally calculated in terms of correlation of static positron emission tomography (PET) measurements across subjects. There is increasing interest in deriving metabolic connectivity at the single-subject level from dynamic PET data, in a similar way to functional magnetic resonance imaging. However, the strong multicollinearity among region-wise PET time-activity curves (TACs), their non-Gaussian distribution, and the choice of the best strategy for TAC standardization before metabolic connectivity estimation, are non-trivial methodological issues to be tackled.**

In this work we test four different approaches to estimate sparse inverse covariance matrices, as well as three similarity-based methods to derive adjacency matrices. These approaches, combined with three different TAC standardization strategies, are employed to quantify metabolic connectivity from dynamic [^{18}F]fluorodeoxyglucose ([^{18}F]FDG) PET data in four healthy subjects.

I. Introduction

In the neuroimaging community, there is interest in developing methods to estimate metabolic connectivity (MC) from [^{18}F]fluorodeoxyglucose ([^{18}F]FDG) positron emission tomography (PET). Instead of exploiting the temporal information of dynamic PET, however, most of the studies have used conventional static measures to derive group-level MC as the covariance of metabolic information across subjects [1][2]. This is in contrast with other imaging modalities, such as functional magnetic resonance imaging (fMRI), where functional connectivity (FC) matrices are built at the single-subject level from zero-lag temporal correlations between the signals' time series [3].

While approaches like Pearson's correlation and independent component analysis (ICA) have been employed to derive MC both with static PET (see [4] for a review) and in the few research works with dynamic PET [5][6], the sparse inverse covariance estimation (SICE) framework has only been applied to static PET so far [1]. SICE is a promising approach, as it infers only direct connections, providing parsimonious and interpretable graphs, and it has already been tested for fMRI FC estimation [3].

Handling dynamic PET data, however, comes with peculiar challenges as compared to fMRI or static PET: 1) the strong multicollinearity amongst time activity curves (TACs) makes the sample covariance singular and not positive semidefinite; 2) TACs are not normally distributed in time, which is an issue for SICE methods, since they are based on the use of L_1 penalty for Gaussian Graphical Models [7]. Moreover, there is no gold standard for TAC standardization [5][6].

We here compared different standardization strategies and algorithms capable of retrieving MC, i.e., subject-level undirected adjacency matrices, using dynamic [^{18}F]FDG PET data from four healthy individuals.

In addition, as estimating MC requires to parcel the brain into regions of interest, we assessed the impact of the parcellation scheme, employing both an anatomical [8] and a fMRI-based atlas [9].

The MC matrices were compared in terms of graph structure, across-subject reproducibility and similarity to a structural connectivity (SC) template.

II. Materials and Methods

A. PET data acquisition and preprocessing

Four healthy subjects (4 males, 51.2 ± 20.8 years old) underwent simultaneous PET/MRI acquisitions on a Siemens 3T Biograph mMR (Siemens Medical Solutions USA, Inc.), equipped with a 16-channel head/neck coil, at the Nuclear Medicine Unit, University Hospital of Padova, Italy.

After bolus injection of 244 ± 22 MBq of [^{18}F]FDG, dynamic PET data were acquired in list mode for 55 minutes. The off-line PET reconstruction was performed with the Siemens e7-tool and comprised attenuation correction, scatter, dead time and decay correction, ordinary Poisson ordered subset expectation maximization (OP-OSEM) with 3 iterations and 21 subsets. The attenuation map was estimated from the patient's T1w structural image as in [10]. The chosen reconstruction grid consisted of 34 frames of increasing duration (10x6s, 8x15s, 7x60s, 9x300s). Images were reconstructed as 256x256x127 matrices (voxel size 2.8 x 2.8 x 2 mm). No spatial smoothing was applied.

The subject's structural scan consisted in a 3D T1w Magnetization Prepared-Rapid Gradient Echo (MPRAGE, TR/TE 2400/3.2 ms, voxel size 1x1x1mm^3). T1w images were bias field corrected, skull stripped, and segmented into grey matter, white matter, and cerebrospinal fluid, and the segmentations were linearly mapped from T1w to PET space.

Tommaso Volpi is with the Department of Neuroscience, University of Padova, Padova, Italy, and with the Padova Neuroscience Center, University of Padova, Padova, Italy (corresponding author: +39 049 827 7694; e-mail: tommaso.volpi@phd.unipd.it).

Erica Silvestri is with the Department of Information Engineering, University of Padova, Padova, Italy (e-mail: erica.silvestri@unipd.it).

Maurizio Corbetta is with the Department of Neuroscience and with the Padova Neuroscience Center (e-mail: maurizio.corbetta@unipd.it)

Alessandra Bertoldo is with the Department of Information Engineering and with the Padova Neuroscience Center (e-mail: alessandra.bertoldo@unipd.it).

Partial volume effects were considered negligible as no spatial smoothing has been performed and PET signals have been extracted only from voxels within the gray matter segmentation. Dynamic PET was motion-corrected using an in-house combination of PMOD (www.pmod.com) and FSL's *mcflirt* [11].

The voxel-wise PET TACs were parcellated according to the AAL2 anatomical atlas [8] (the last 8 parcels, which belong to the cerebellum, were discarded for small size), and the Schaefer cortical atlas [9] (100 cortical regions), supplemented by 12 subcortical regions delineated by Freesurfer [12]. For both atlases, the total number of parcels amounted to 112.

The first 10 frames (60 s) of the parcel-wise PET TACs were discarded, due to high noise content; the remaining frames were interpolated on a uniform virtual grid (15 s step), obtaining a subject-wise matrix $\boldsymbol{X} \in \mathbb{R}^{p \times T}$, where p is the feature size (112 parcels) and T is the sample size (216 time points).

B. Data standardization

The parcel-wise TACs were standardized as follows:

1) A matrix $\boldsymbol{X}_Z$ is obtained by z-scoring $\boldsymbol{X}$: each column of $\boldsymbol{X}$ is centered to have mean 0 and scaled to have standard deviation 1 (i.e., subtracting the global mean and dividing for its standard deviation). Subsequently, $\boldsymbol{X}_{ZT}$ is generated by subtracting the mean from each row (i.e., removing the parcel's mean);

2) A matrix $\boldsymbol{X}_S$ is obtained by subtracting the mean from each column of $\boldsymbol{X}$. Subsequently, $\boldsymbol{X}_{SZ}$ is generated by z-scoring $\boldsymbol{X}_S$: each row of $\boldsymbol{X}_S$ is centered to have mean 0 and scaled to have standard deviation 1;

3) A matrix $\boldsymbol{X}_M$ is obtained by dividing each row of $\boldsymbol{X}$ by the mean across rows of $\boldsymbol{X}$, as in [5][6].

C. Similarity-based approaches

Three pairwise similarity metrics were derived from the standardized data $\boldsymbol{X}_{ZT}, \boldsymbol{X}_{SZ}, \boldsymbol{X}_M$, as for FC [13].

First, the bivariate Pearson's correlation coefficient **r** [6] was calculated between each pair of rows of $\boldsymbol{X}$. Secondly, the pairwise Euclidean distance was computed between each pair of rows of $\boldsymbol{X}$ and rescaled to the [0;1] range, then its complement to 1 was calculated as a similarity metric.

Thirdly, cosine similarity was calculated as:

$$CosSim = \frac{X_i X_k}{\|X_i\| \|X_k\|} = \frac{\sum_{t=1}^{T} x_{it} x_{kt}}{\sqrt{\sum_{t=1}^{T} x_{it}^2} \sqrt{\sum_{t=1}^{T} x_{kt}^2}} \quad (1)$$

where $X_h = (x_{h1}, x_{h2}, .., x_{hT})'$, for h = 1, …, p.

D. Sparse inverse covariance estimation (SICE) methods

Gaussian Graphical Models assume that the T observations for every feature p follow a multivariate normal distribution with mean vector $\mu_p \in \mathbb{R}$ and covariance matrix $\boldsymbol{\Sigma} \in \mathbb{R}^{p \times p}$. The precision matrix $\boldsymbol{\Theta} = \boldsymbol{\Sigma}^{-1}$ is the inverse of $\boldsymbol{\Sigma}$, and can be represented by an undirected graph with p nodes, i.e., the 112 parcels, and $p \times p$ edges, which capture conditional dependence amongst the parcels. A partial correlation matrix $\boldsymbol{\Pi}$ can then be derived from $\boldsymbol{\Theta}$ by standardization:

$$\Pi_{(i,k)} = -\frac{\Theta(i,k)}{\sqrt{\Theta(i,i)\Theta(k,k)}} \quad \text{for i= 1, …, p and k= 1, …, p} \quad (2)$$

Before employing SICE, the sample covariance $\boldsymbol{S} \in \mathbb{R}^{p \times p}$ was calculated for $\boldsymbol{X}_{ZT}, \boldsymbol{X}_{ST}, \boldsymbol{X}_M$. With high multicollinearity (reciprocal condition number ≅ 0), $\boldsymbol{S}$ is singular, non-Positive Definite (PD), and not invertible. To address this, the nearest PD alternating projection method [14] was used to enforce positive semi-definiteness by finding the closest positive semi-definite matrix $\boldsymbol{S}_{PSD}$ to the covariance in terms of Frobenius norm: $\boldsymbol{S}_{PSD} = \min_{\boldsymbol{S} \succeq 0} \| \boldsymbol{S} - \widehat{\boldsymbol{S}} \|_F$.

Higham's algorithm was implemented with the function *nearPD* from the R (www.r-project.org/) package *Matrix*.

The *graphical LASSO* (GLASSO) [7] estimates $\boldsymbol{\Theta}$ by maximizing the following objective function

$$\widehat{\Theta} = \underset{\Theta \succ 0}{\operatorname{argmax}} (\log(\det \Theta) + tr(S\Theta) - \lambda \|\Theta\|) \quad (3)$$

where *tr* is the trace, $\boldsymbol{\Theta} \succ 0$ denotes that $\boldsymbol{\Theta}$ is PD, *det* is the determinant, and λ is the regularization parameter.

Four SICE approaches based on L_1 regularization of the log-likelihood of a multivariate Gaussian distribution were selected:

- The *DP-GLASSO* algorithm [15] was chosen as it exhibits monotone behavior in maximizing the objective function, does not have convergence issues, and has PD solution. The *GLassoElnetFast* [16] R package implementation was used.
- The *nonparanormal truncated* approach [17] transforms $\boldsymbol{X}$ into a multivariate Gaussian latent variable Z_{ij}, by means of $\boldsymbol{\Phi}$, which is a smooth, monotone function used to transform $\boldsymbol{X}$'s marginal distributions. Here, $\boldsymbol{\Phi}$ was chosen as the truncated empirical cumulative distribution function and computed with the R package *huge* [18]. The covariance of the transformed data was used as input for DP-GLASSO.
- The *skeptic* method ("**S**pearman/**K**endall **E**stimates **P**reempt **T**ransformations to **I**nfer **C**orrelation") [19] computes the covariance matrix as $\hat{\Sigma}^{\rho} = (\hat{\sigma}_{ik}^{\rho})$ with $(\hat{\sigma}_{ik}^{\rho}) = 2 * \sin(\frac{\pi}{6} \hat{\rho}_{ik})$ as the Spearman's ρ rank-based covariance estimator. The *skeptic* estimation of the covariance matrix was implemented with the R package *huge* [18], and then subjected to the DP-GLASSO algorithm.
- γ-*LASSO* is a robust SICE estimator based on the γ-divergence [20]. For $\gamma = 0$, the solution is equal to GLASSO's, for higher values a weighted form of GLASSO is deployed, with observations weighted as outliers if their likelihood is small. γ-LASSO has always PD solution, its bias is small, and performs well for skewed distributions and high presence of outliers. However, as the optimization problem is non-convex, the computational process is time consuming. γ-LASSO was implemented with the R package *rsGGM* using the DP-GLASSO algorithm [20].

Each $\boldsymbol{\Theta}$ matrix estimated by SICE methods was converted to a partial correlation matrix $\boldsymbol{\Pi}$.

1. Across-subject and across-method reproducibility

Since, as for SC and FC, the MC matrix is expected to be sparse, before comparing the obtained connectivity matrices, a sparsity threshold was applied to retain only 20% of the edges. These sparse matrices, calculated in every subject for each SICE and non-SICE method, and for each standardization method, were then binarized [1]. Moreover,

the median MC matrix across subjects was calculated for each method and thresholded at 20% sparsity.

Pairwise Dice similarity coefficients were used to compare 1) binary MC matrices across subjects, and 2) binary median MC matrices across methods.

B. Modularity of the estimated networks

For all median MC matrices, the associated graph modularity was assessed by means of the Louvain's community detection method [21], with a resolution parameter varying across a linearly spaced grid of values (from 0.9 to 1.75, with 0.05 step). Finally, the modularity metric, Q, was employed to compare community structure across graphs.

C. Comparison with structural connectivity

A publicly available tractography atlas was used to create a group-level SC matrix [22]. This resulted in two 112x112 SC adjacency matrices (one for each parcellation scheme) whose entries represent the number of white matter tracts between each pair of the 112 selected parcels. As for MC, the sparsity level of the matrix was set to ~20%.

To assess the agreement between the estimated direct metabolic connections and the underpinning structural connections, the Dice similarity between binarized SC and each binary median MC network was computed.

III. Results

A representative selection of the median MC matrices, which were extracted for the seven estimation methods, three standardizations and two atlases, is shown in **Fig. 1**. From visual inspection, the LH-RH structure with clearly distinguishable inter-hemispheric homotopic connections is apparent in most methods. Additionally, the γ-LASSO matrix for standardization $\boldsymbol{X}_{SZ}$ *(first row, second from the left)* shows marked block-diagonal structure with strong connectivity within each subnetwork.

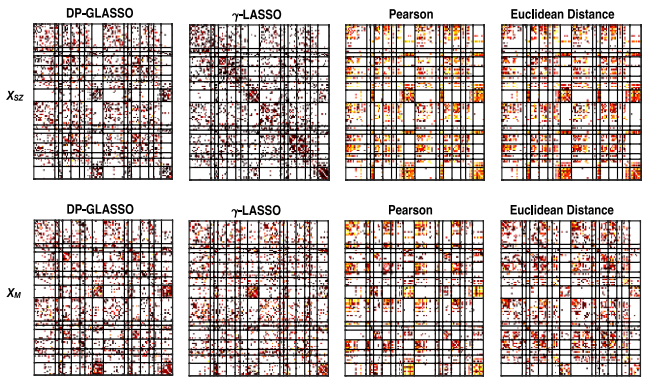

Fig. 1: Median MC matrices for 4 estimation methods (DP-GLASSO, γ-LASSO, Pearson's correlation and Euclidean Distance) and 2 standardization approaches ($\boldsymbol{X}_{SZ}, \boldsymbol{X}_{M}$), the AAL2 atlas. Each symmetric matrix is organized into 4 blocks: left upper block, as the connectivity between left hemisphere (LH) regions; right lower block, as the connectivity between right hemisphere (RH) regions; left lower block and right upper block, as connections between LH and RH. Additional subdivisions (*black grid*) represent subnetworks of regions. Edges around the main diagonal represent within-subnetwork connectivity, the secondary diagonals (left lower and right upper blocks) instead represent inter-hemispheric homotopic connections.

For what concerns Louvain's Q values of the median MC matrices, while SICE methods' modularity structure is insensitive to the different values of the resolution parameter ($\mu \pm \sigma = 0.25 \pm 0.003$), non-SICE methods display decreasing Q values as the resolution parameter becomes higher ($max = 0.4$; $min = 0.1$).

When assessing across-subject reproducibility, Dice similarity for SICE methods is low-moderate (0.3-0.4), while non-SICE methods have significantly higher Dice (0.5-0.6) for all standardizations (**Fig. 2**). Both the AAL2 and Schaefer atlas demonstrate the same pattern, but standardization $\boldsymbol{X}_{SZ}$ leads to higher Dice values for SICE methods with Schaefer ($\mu \pm \sigma = 0.3 \pm 0.02$), with clearer distinction from $\boldsymbol{X}_{ZT}$ ($\mu \pm \sigma = 0.23 \pm 0.02$) and $\boldsymbol{X}_{M}$ ($\mu \pm \sigma = 0.24 \pm 0.02$).

The across-method similarity of median MC matrices, assessed with Dice, showed that SICE and non-SICE methods are clustered separately, especially for standardization $\boldsymbol{X}_{SZ}$ (*not shown*).

For what concerns the MC-SC similarity, the non-SICE methods have higher Dice values (0.3-0.4) than the SICE methods (0.2-0.3). This is true especially for AAL2 (**Fig. 3**), while for Schaefer the difference is weaker (*not shown*).

IV. Discussion

The aim of this work was to derive MC from dynamic [^{18}F]FDG PET at the single-subject level, with focus on network characterization and data standardization.

The main issues to be faced in MC estimation are related to the non-Gaussianity and multicollinearity of dynamic PET. The first problem was tackled by comparing methods designed for a bivariate or multivariate Gaussian context (Pearson's correlation, Cosine Similarity, DP-GLASSO) to other approaches (truncated, skeptic, γ-LASSO, Euclidean distance) designed for data with heavy-tailed distribution and high outlier contamination. The multicollinearity of the input data, leading to singular covariance $\boldsymbol{S}$, was handled using the DP-GLASSO algorithm [15] for all SICE methods, to guarantee a PD estimate of $\boldsymbol{\Theta}$, together with Dykstra's correction [14]. However, the second group of methods did not seem to provide better reproducibility or a good match with the underlying structure than their parametric counterparts.

As for data standardization, we tested approaches aimed at highlighting different characteristics of the signal: while methods 1) and 3) evaluate the fluctuations around the metabolic baseline, as in [5][6], method 2) emphasizes the fluctuations of the signal with respect to itself.

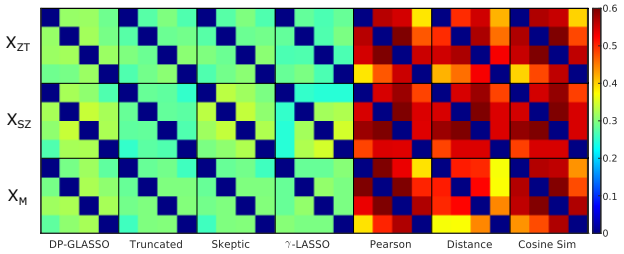

Fig. 2: Across-subject Dice Similarity values for binarized MC matrices (20% sparsity), AAL2 atlas. Each 4x4 block represents the similarity between subjects (n = 4) for a given estimation (rows) and standardization (columns) method.

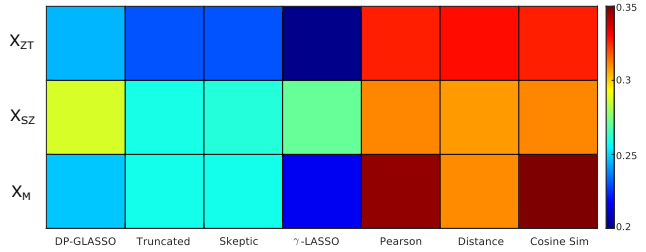

Fig. 3: Dice similarity between binarized SC and median MC matrices (20% sparsity) for all standardization (rows) and MC estimation (columns) methods, AAL2 atlas.

Since no gold standard is available, one must remember that non-trivial differences in MC networks emerge with different standardization methods.

It should be noted that the PET data, reconstructed with a 34-frame time grid, was subjected to virtual grid interpolation. This is different from previous studies with dynamic PET MC, where a uniform grid was employed directly for data reconstruction [5][6]. We believe that the approach used here is faithful to the PET count statistics, whose noise variance changes considerably across the scan, and thus more appropriate for MC estimation.

Finally, the biological interpretation of dynamic PET MC is still under debate, as it is likely to be strongly driven by pharmacokinetic aspects of tracer distribution and absorption [2][6]. Regarding this, future work should explore how these results relate to constant infusion functional [^{18}F]FDG PET, from which MC has also been estimated [23].

V. Conclusion

We presented two class of methods (SICE and non-SICE) that can be used to derive MC networks from dynamic [^{18}F]FDG PET data at the single-subject level. Pearson's correlation, Euclidean distance and Cosine Similarity (i.e., non-SICE methods) provide better results for between-subject reproducibility and similarity to SC.

Notably, most methods succeeded in retrieving a similar network structure, with consistent identification of inter-hemispheric and homotopic connections which are expected from brain connectivity studies. The choice of the standardization method for PET TACs leads to non-trivial differences between networks.

Future work should expand on these findings by employing different SICE algorithms (non-convex penalties, Bayesian methods, Graphical Elastic Net [16]) and investigating MC estimation for other PET tracers.

Acknowledgment

The authors would like to thank Dr. Diego Cecchin, M.D., Dr. Fabio Magnani, M.D., and Dr. Silvia Facchini, Ph.D., for their role in the acquisition of the data.

References

[1] S. Huang, J. Li, L. Sun, J. Ye, A. Fleisher, T. Wu, K. Chen, E. Reiman, and the Alzheimer's Disease Neuroimaging Initiative, "Learning brain connectivity of Alzheimer's disease by sparse inverse covariance estimation", *NeuroImage*, vol. 50, no. 3, pp. 935–949, Apr. 2010.

[2] M. Veronese *et al.*, "Covariance statistics and network analysis of brain PET imaging studies," *Sci. Rep.*, vol. 9, no. 1, 2496, Feb. 2019.

[3] S. Smith *et al.*, "Network modelling methods for fMRI", *NeuroImage*, vol. 54, pp. 875-891, Jan. 2011.

[4] I. Yakushev, A. Drzezga, and C. Habeck, "Metabolic connectivity: methods and applications", *Curr. Opin. Neurol.*, vol. 30, no. 6, pp. 677-685, Dec. 2017.

[5] D. G. Tomasi *et al.*, "Dynamic brain glucose metabolism identifies anti-correlated cortical-cerebellar networks at rest," *J. Cereb. Blood Flow Metab.*, vol. 37, no. 12, pp. 3659-3670, Dec. 2017.

[6] A. M. Amend, T. M. Ionescu, X. Di, B. J. Pichler, B. B. Biswal, and H. F. Wehrl, "Functional resting-state brain connectivity is accompanied by dynamic correlations of application-dependent [^{18}F]FDG PET-tracer fluctuations, *NeuroImage,* vol. 196, pp. 161-172, Aug. 2019.

[7] J. Friedman, T. Hastie, and R. Tibshirani, "Sparse inverse covariance estimation with the graphical lasso," *Biostatistics*, vol. 9, no. 3, pp. 432–441, July 2008.

[8] E. T. Rolls, M. Joliot, and N. Tzourio-Mazoyer, "Implementation of a new parcellation of the orbitofrontal cortex in the automated anatomical labeling atlas," *NeuroImage*, vol. 122, pp. 1–5, 2015.

[9] A. Schaefer *et al.*, "Local-global parcellation of the human cerebral cortex from intrinsic functional connectivity MRI", *Cereb Cortex*, vol. 28, no. 9, pp. 3095-3114, Sep. 2018.

[10] D. Izquierdo-Garcia *et al.*, "An SPM8-based approach for attenuation correction combining segmentation and nonrigid template formation: application to simultaneous PET/MR brain imaging", *J. Nucl. Med.*, vol. 55, no. 11, pp. 1825-1830, Nov. 2014.

[11] M. Jenkinson, P. Bannister, M. Brady, and S. Smith, "Improved Optimization for the Robust and Accurate Linear Registration and Motion Correction of Brain Images," *NeuroImage*, vol. 17, no. 2, pp. 825–841, 2002.

[12] B. Fischl *et al.*, "Whole brain segmentation: automated labeling of neuroanatomical structures in the human brain", *Neuron*, vol. 33, no. 3, pp. 341-355, Jan. 2002.

[13] R. Mohanty, W. A. Sethares, V. A. Nair, and V. Prabhakaran, "Rethinking Measures of Functional Connectivity via Feature Extraction," *Scientific Reports*, vol. 10, no. 1, 2020.

[14] N. J. Higham, "Computing the nearest correlation matrix-a problem from finance," *IMA Journal of Numerical Analysis*, vol. 22, no. 3, pp. 329–343, July 2002.

[15] R. Mazumder and T. Hastie, "The graphical lasso: new insights and alternatives," *Electron. J. Stat.*, vol. 6, pp. 2125-2149, Nov. 2012.

[16] S. Kovács, T. Ruckstuhl, H. Obrist, and P. Bühlmann, "Graphical Elastic Net and Target Matrices: Fast Algorithms and Software for Sparse Precision Matrix Estimation," 2021, http://arxiv.org/abs/2101.02148.

[17] H. Liu, J. Lafferty, and L.A. Wasserman, "The nonparanormal: semiparametric estimation of high dimensional undirected graphs", *J. Mach. Learn. Res.*, vol. 10, pp. 2295-2328, Oct. 2009.

[18] T. Zhao, H. Liu, K. Roeder, J. Laffety, and I. Wasserman, "The huge package for high-dimensional undirected graph estimation in R", *J. Mach. Learn. Res.,* vol. 13, pp. 1059-1062, Dec. 2012.

[19] H. Liu, F. Han, M. Yuan, J. Lafferty, and L.A. Wasserman, "High-dimensional semiparametric Gaussian copula graphical models", *Ann. Statist.*, vol. 40, pp. 2293-2326, Aug. 2012.

[20] K. Hirose, H. Fujisawa, and J. Sese, "Robust sparse Gaussian graphical modeling", *J. Multivariate Anal.*, vol. 161, pp. 172-190, Sep. 2017.

[21] P. J. Mucha, T. Richardson, K. Macon, M. A. Porter, and J.-P. Onnela, "Community Structure in Time-Dependent, Multiscale, and Multiplex Networks," *Science*, vol. 328, no. 5980, pp. 876–878, 2010.

[22] F.-C. Yeh *et al.*, "Population-averaged atlas of the macroscale human structural connectome and its network topology," *NeuroImage*, vol. 178, pp. 57–68, 2018.

[23] S. Li, S. Jamadar, P. G..D. Ward, M. Premaratne, G. F. Egan, and Z. Chen, "Analysis of continuous infusion functional PET (fPET) in the human brain," *Neuroimage*, vol. 213, 116720, June 2020.